Modelling a Multilevel LCC Resonant AC-DC Converter for Wide Variations in the Input and the Load

Juan A. Martín-Ramos, *Member, IEEE*, Óscar Pardo-Vaquero, Juan Díaz, *Member, IEEE*, Fernando Nuño, *Member, IEEE*, Pedro José Villegas, *Member, IEEE*, and Alberto Martín-Pernía, *Member, IEEE*

***Abstract*—Several applications need a high power, high output voltage ac/dc converter. The structure includes a dc/dc resonant stage, which is fed from a three-phase line. Due to standards, rectified dc input voltage varies largely from 400 to 750 V affecting the adversely overall design and current levels. In fact, losses in the inverter become unbearable if both switching frequency and transferred power are desired beyond a certain level. In those cases, it is necessary to connect several switches in parallel. As an alternative, the new switches can configure a new modular structure instead, adding more flexibility in the control to compensate input voltage variations. As a result, the required circulating current is reduced to a half, with benefits in total power losses. Moreover, the nature of the topology allows a reconfiguration of the resonant net (LCC) for low power, reducing even further the minimum circulating current under those conditions (fluoroscopy, for instance). In this paper, the new multilevel resonant topology is mathematically modeled and proposed for radiography and fluoroscopy. An example illustrates the design procedure for a given application at 100 kW, 50–150 kV.**

***Index Terms*—AC/DC power conversion, high voltage techniques, power system modeling, resonant power conversion.**

I. Introduction

A SIGNIFICANT number of industrial applications require a power supply capable to deliver a dc voltage of tens of kV while transferring a power of tens of kW. Such applications include X-ray generators, electron beam welding machines, or electrostatic precipitators to name a few [1]–[5]. In all cases, the primary power supply is a three-phase line. Universal power input ranges from 380–480 V rms depending on the different regional regulations. Fig. 1 shows a block diagram with the usual structure of such a high-voltage power supply. The first stage is a three-phase rectifier. Given the different line settings, operating tolerances and 50–60 Hz ripple [6], the rectifier output can take values between 400 V and 750 V. The second stage is a square wave inverter where the switching frequency is in the range of tens of kHz. This value is high enough to consider its input voltage as dc and to allow the minimization of the transformer size.

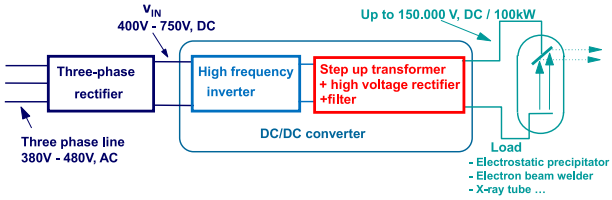

Fig. 1. Block diagram of a high voltage power supply.

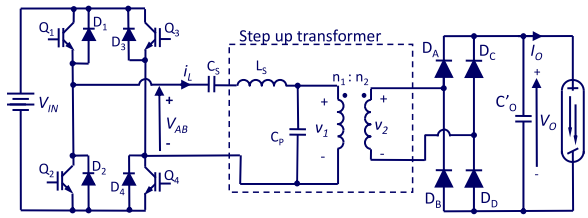

Fig. 2. Full-bridge PRC-LCC resonant topology with a capacitor as output filter. V_{AB} is the inverter output voltage and i_{L} is the current through the resonant inductor L_{S}.

Transformer design is certainly the cornerstone for these kinds of power supplies. It provides electrical isolation and raises the output voltage to the required range: between 20 kV and 150 kV, depending on the application. Its special features can be summarized in two noticeable consequences for the topology: the presence of a leakage inductance, LS, and a stray capacitance in the secondary, C_P; both significant [7]–[9]. The transformer also presents a magnetizing inductance in parallel with C_P, but it can be neglected because, in the switching frequency range, its impedance is at least 10 times bigger than the capacitor's impedance. In general, the inclusion of a stepup transformer in the circuit leads to resonant topologies [10]–[23]. In particular, the series parallel resonant topology, PRC-LCC, with a capacitor as output filter is one of the most attractive solutions, since it includes the transformer parasitic elements easily, Fig. 2 [16]–[21]. This paper presents a multilevel modification of this topology, which provides further versatility.

Manuscript received February 26, 2018; revised May 11, 2018 and July 13, 2018; accepted August 12, 2018. Date of publication August 26, 2018; date of current version April 20, 2019. This work was supported by the Spanish Government with the actions TEC2014-53324-R and TEC2016-77738-R. Recommended for publication by Associate Editor I. Barbi. *(Corresponding author: Juan A. Martín-Ramos.)*

The authors are with the Edificios Departamentales Oeste, Universidad de Oviedo, Gijón 33204, Spain (e-mail:

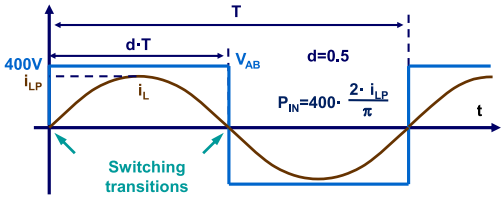

Fig. 3. Inverter voltage V_{AB} and resonant current i_{L} for maximum transferable power at minimum input voltage, 400 V, in an ideal design.

II. Resonant Inverter

A full-bridge based PRC-LCC resonant converter, Fig. 2, must be capable of providing full power with the minimum input voltage, 400 V. The best design strategy is to employ a large duty cycle and a close-to-resonance switching frequency for these conditions. Fig. 3 shows the ideal aspect of the resonant current i_L and the inverter output voltage V_{AB} at minimum input voltage and rated output power. The inverter is delivering power to the load throughout the period. Therefore, the absence of reactive energy minimizes the required amplitude of the resonant current i_{LP}. This situation is truly advantageous also from the viewpoint of the switching losses, because the switching transitions always occur without current. As an example, in a 100 kW rated power supply, an energy balance shows that the minimum required current peak i_{LP} in ideal conditions, will be around 400 A (1) if $V_{\mathrm{IN}} = 400$ V. In practice, it would be higher since converter power losses must be compensated and 0.5 as the duty cycle is not always possible

$$P_{\mathrm{IN}} = V_{\mathrm{IN}} \cdot \frac{2 \cdot i_{\mathrm{LP}}}{\pi} \rightarrow i_{\mathrm{LP}} = \frac{\pi \cdot P_{\mathrm{IN}}}{2 \cdot V_{\mathrm{IN}}} \sim 400\,\mathrm{A}. \qquad (1)$$

Obviously, when the input voltage is not minimum the working regime must change to maintain transferred power. Many control possibilities arise: to increase the switching frequency above resonance, Fig. 4(a), to decrease the duty cycle, Fig. 4(b), or to combine both strategies, Fig. 4(c). In all the cases, ideal conditions as in Fig. 3 are no longer possible if $V_{\mathrm{IN}} > 400$ V and higher V_{IN} is not translated into a diminishing current amplitude like desired. Fig. 4 includes a mathematical approach to calculate that amplitude in every case.

This paper proposes a new power topology to improve the design of high voltage, high power dc–dc converters. The introduction of a modular configuration of the inverter, Fig. 5, allows a better design of the resonant tank, reducing the resonant current peak to a half. The switching transitions are separated into two, taking place in a better situation for the IGBTs, and reducing overall losses. The higher flexibility of the topology also allows a much better operation when the power supply must deliver very low power. In X-ray medical applications, this situation appears in diagnosis through fluoroscopy and it is very important to asses overall performance. Again, for low power, the original PRC-LCC resonant topology presents current levels even four times higher than the proposed solution.

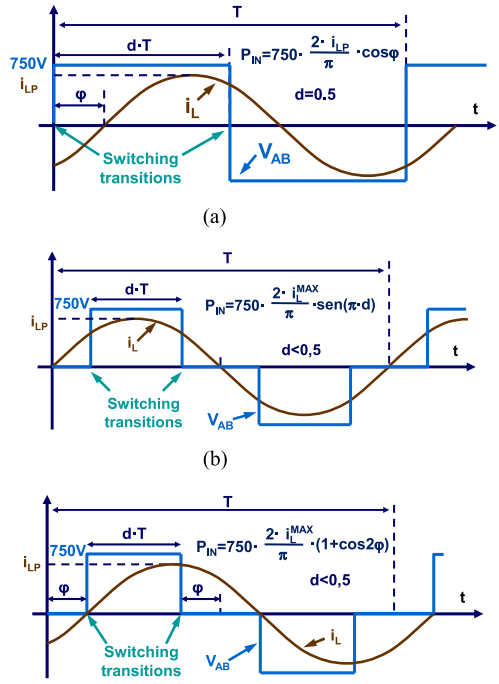

Fig. 4. Possibilities of the control to maintain full power when the input voltage is not minimum. The resonant current, i_{L}, and the inverter output voltage V_{AB} are represented. (a) Switching frequency is increased while duty cycle remains constant. (b) Duty cycle is reduced at resonant frequency. (c) One of the possibilities when modifying both switching frequency and duty cycle.

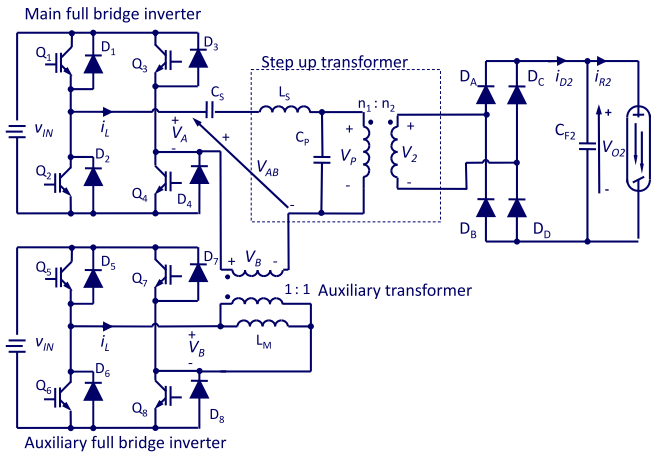

Fig. 5. Circuit for the proposed multilevel topology.

III. Multilevel PRC-LCC Resonant Converter

The proposed topology couples two full-bridges through an auxiliary transformer with a 1:1 ratio, Fig. 5. As there are two inverters, there are also two duty cycles d_1 and d_2 and a new control parameter is gained. Now, the voltage at the input of the resonant tank V_{AB} maintains a square waveform, but presents five voltage levels. As Fig. 6 shows, V_{AB} can look different depending on the timing between inverters. The designer should choose according to the switching losses in the inverter. The option represented in Fig. 6(b) looks like an extension of Fig. 4(c) control strategy. It minimizes circulating energy and ensures a

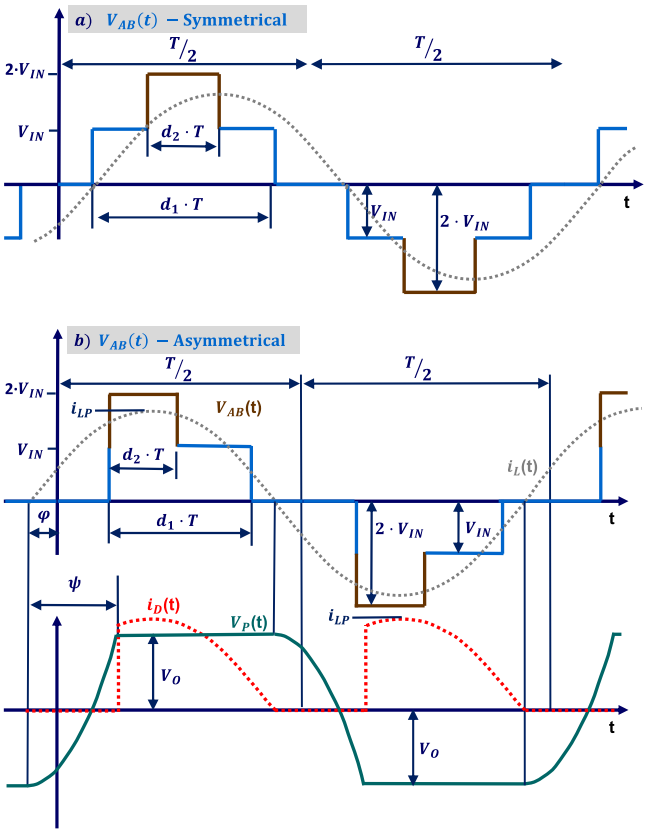

Fig. 6. Two of the possibilities for $V_{\mathrm{AB}}(t)$. The main inverter is injecting voltage during $d_1 \cdot T$, the auxiliar inverter during $d_2 \cdot T$. (a) Symmetrical appearance. (b) Assymetrical appereance towards the left. The waveforms represent: Output voltage of the inverters V_{AB} and resonant current, i_{L}. Only for asymmetrical operation: voltage at the parallel capacitor V_{P} and current after the output rectifier i_{D}.

zero voltage switching during turn ON, which is a more difficult transition in this sort of switches [21]. Now hard turn OFF switching can still happen, but the control can avoid that both of the inverters were involved at maximum current.

On the other hand, the inverter voltage V_{AB} is still applied over a resonant network, and the switching frequency is in the proximity of resonance. Therefore, the first harmonic approximation of currents and voltages provides a simple and convenient mathematical tool for the analysis of the topology. With the multilevel structure of the inverter, two controllable duty cycles provide more flexibility to configure V_{AB}. Now, it is possible to maintain in a narrower range its first harmonic term, compensating better the wide input voltage sweep, 400–750 V. Besides, the applied voltage to the resonant tank is higher, since the peak can reach two times V_{IN}, Fig. 6. Thus, the design of the topology resonant network may consider a higher minimum input voltage V_{IN}. There is a certain degree of freedom in selecting the new minimum V_{IN}, but assuming 800 V, a new evaluation of (1) shows that only about a half of the resonant current is necessary for the same delivered power.

Obviously, a higher voltage at the input affects the design, and the resonant network should change of values. The price to pay for such a flexibility is an auxiliary transformer with a 1:1 ratio. It makes possible the addition of both inverter voltages for high power levels in radiography avoiding the necessity of two isolated inputs. However, the auxiliary transformer has an additional use that improves the behavior of the converter in fluoroscopy. At such low power, the auxiliary full bridge can be kept open, and the magnetizing inductance of the auxiliary transformer L_M appears in the resonant network. Added to the leakage inductance, L_S, it modifies the resonant circuit, reducing largely the required current and shifting switching frequency at low power. It is well known that, in resonant topologies, the switching frequency must be increased considerably for low power. Also that the circulating current is not reduced proportionally [22]–[26]. This scheme of a new resonant inductance in the circuit helps to mitigate both effects improving the expected efficiency for fluoroscopy.

IV. Large-Signal Model

Any optimized design of a power source relies on a mathematical model. The large signal model of the proposed topology can be obtained by applying Kirchhoff's laws (KCL and KVL) to it. Starting at the resonant mesh, it presents two forms, depending on whether the auxiliary full bridge inverter is switching or open (fluoroscopy). The difference between both cases lies in the different series inductance of the mesh, L_S or $L_S + L_M$, and the role of d_2 in V_{AB}. The resulting series inductance is referred as L_X. Equation (2) represents the KVL for the topology resonant net. As shown in Fig. 6, the timely definition of V_{AB} depends on V_{IN}, f, d_1, and d_2. If the auxiliary inverter is not used $d_2 = 0$. On its side, r is a lumped resistor to represent the conduction losses in the resonant network.

Of course, there is a relationship between the current and the voltage in the capacitor C_S (3). And finally, balance of current (KCL) at the high-voltage output capacitor leads to (4). There, the current i_D is divided between the output capacitor C_F and the load, which behaves as a resistor R. Magnitudes in (4) have been transferred to the primary of the step-up transformer

$$V_{\mathrm{AB}}(t) = V_S(t) + V_P(t) + L_X \cdot \frac{di_L(t)}{dt} + r \cdot i_L(t) \tag{2}$$

$$C_S \cdot \frac{dV_S(t)}{dt} = i_L(t) \tag{3}$$

$$i_D = C_f \frac{dV_O(t)}{dt} + \frac{V_O(t)}{R}. \tag{4}$$

These three differential equations (2)–(4) are the state equations. They form a dynamical model for the topology. They include three variables that store a significant amount of energy: V_S, V_O, and i_L. These three variables are the state variables. As the variation of energy is important in the circuit state analysis, their time-derivatives appear explicitly in the state equations. In the resonant side of the topology, the waveforms are periodic, Fig. 6. Although the voltages V_{AB} and V_P have linear lapses, the expected current is quasi-sinusoidal. Therefore, i_L and V_S can be approximated by its first harmonic term in the Fourier series without substantial accuracy loss (5) and (6) [27]. This affects the state equations (2) and (3). However, the only state variable in (4) is V_O. In the lapse of a switching period, it is expected to be a dc voltage with narrowed ripple. Therefore, it is possible

to approximate it by the dc term of its Fourier series, an average voltage which can vary in the long run (7)

$$i_L(t) \sim i_{\mathrm{LA}}(t) \cdot \sin(\omega t) + i_{\mathrm{LB}}(t) \cdot \cos(\omega t) \tag{5}$$

$$V_S(t) \sim V_{\mathrm{SA}}(t) \cdot \sin(\omega t) + V_{\mathrm{SB}}(t) \cdot \cos(\omega t) \tag{6}$$

$$V_O(t) \sim V_{\mathrm{OAVG}}(t). \tag{7}$$

It should be noted that although V_P is the voltage of a capacitor, the energy that it represents is not significant, and hence it is not a state variable. In fact, its voltage is clamped twice every period, when the output rectifier is ON, by the voltage at C_f, a quite higher capacitance. Actually, the output rectifier operates in discontinuous conduction mode, being OFF every time the resonant current i_L changes its sign. At that momento of the period, i_L flows through C_P, charging it sinusoidally. After some time, V_P reaches V_O and the rectifier is ON again. Now C_f and C_P are connected in parallel. Given the high capacitance of C_f, the resonant current can hardly change the voltage across this capacitor, and it can be assumed to remain constant: V_P is clamped at V_O. This process is repeated twice a period, Fig. 6(c). The conduction angle of C_P in a period, ψ, can be deduced from the differential equation of a charging capacitor. Considering the resonant current as sinusoidal (5), ψ is expressed as a function of the current peak i_{LP} and the value of the output voltage referred to the primary V_O, (8), or in other words, as a function of two state variables

$$\cos\psi = 1 - \frac{2 \cdot \omega C_P \cdot V_O}{i_{\mathrm{LP}}} = 1 - \frac{2 \cdot \omega C_P \cdot V_O}{\sqrt{i_{\mathrm{LA}}^2 + i_{\mathrm{LB}}^2}}. \tag{8}$$

Fig. 6(b) shows that the formulation of $V_P(t)$ and $i_D(t)$ depend on $\psi(t)$, and in consequence, on $i_{\mathrm{LA}}(t)$, $i_{\mathrm{LB}}(t)$, and $V_O(t)$. $V_P(t)$ appears in (2), a state equation for the resonant net. Applying the extended describing function technique [28], the first harmonic term is a good approximation not only for the state variables (5) and (6) but also for the others V_P (9) and V_{AB} (10). Applying the same criteria to (4), the average value is a good approximation for $i_D(t)$ (11)

$$V_P(t) \sim V_{\mathrm{PA}}(t) \cdot \sin(\omega t) + V_{\mathrm{PB}}(t) \cdot \cos(\omega t) \tag{9}$$

$$V_{\mathrm{AB}}(t) \sim V_{\mathrm{ABA}}(t) \cdot \sin(\omega t) + V_{\mathrm{ABB}}(t) \cdot \cos(\omega t) \tag{10}$$

$$i_D(t) \sim \frac{i_{\mathrm{LP}}(t)}{\pi} \cdot (1 + \cos[\psi(t)]) \tag{11}$$

where $\mu(t)$, $V_{\mathrm{PA}}(t)$, and $V_{\mathrm{PB}}(t)$ are abbreviations given by (12)–(14), respectively

$$\mu(t) = \psi(t) - \sin[\psi(t)] \cdot \cos[\psi(t)] \tag{12}$$

$$V_{\mathrm{PA}}(t) = \frac{i_{\mathrm{LA}}(t) \cdot \sin^2[\psi(t)] + i_{\mathrm{LB}}(t) \cdot \mu(t)}{\pi \cdot \omega C_P} \tag{13}$$

$$V_{\mathrm{PB}}(t) = \frac{i_{\mathrm{LB}}(t) \cdot \sin^2[\psi(t)] - i_{\mathrm{LA}}(t) \cdot \mu(t)}{\pi \cdot \omega C_P}. \tag{14}$$

However, the expresions $V_{\mathrm{ABA}}(t)$ and $V_{\mathrm{ABB}}(t)$ depend on the way the signals of both inverters are added. In this paper, two particular options are annalyzed. The Fourier coefficients are given in (15)–(18), respectively, for the symmetrical, Fig. 6(a), and asymetrical, Fig. 6(b) configurations. In all the cases, d_1 is the duty cycle of the main inverter and d_2 is the duty cycle of the auxiliary inverter. If the transferred power is low enough (fluoroscopy, for instance) this auxiliary inverter is not operating. In this case, (15)–(18) are still valid, but $d_2 = 0$

$$V_{\mathrm{ABA}}(t) = \frac{4 \cdot V_{\mathrm{IN}}}{\pi} \cdot [\sin(\pi d_1) + \sin(\pi d_2)] \tag{15}$$

$$V_{\mathrm{ABB}}(t) = 0 \tag{16}$$

$$V_{\mathrm{ABA}}(t) = \frac{2 \cdot V_{\mathrm{IN}}}{\pi} \cdot [3\sin(\pi d_1) - \sin(\pi d_1 - 2\pi d_2)] \tag{17}$$

$$V_{\mathrm{ABB}}(t) = \frac{2 \cdot V_{\mathrm{IN}}}{\pi} \cdot [-\cos(\pi d_1) + \cos(\pi d_1 - 2\pi d_2)]. \tag{18}$$

Now, the state equations (2)–(4) can be reconsidered to substitute the state variables (5)–(7), and other variables V_P, i_D, and V_{AB} (9)–(11) for their suitable harmonic approximation. This substitution modifies the mathematical expression of the dynamic model (19)–(23).

1) All the terms in (2) and (3) contain sin (ωt) or cos (ωt). Grouping them in separate families, (2) is split into two equations: (19) and (20). Likewise (3) gives place to (21) and (22). Therefore, there are five state equations now.
2) The new number of variables increases to five. They are: $i_{\mathrm{LA}}(t)$, $i_{\mathrm{LB}}(t)$, $V_{\mathrm{SA}}(t)$, $V_{\mathrm{SB}}(t)$, and $V_{\mathrm{OAVG}}(t)$. The other variables of the original model have been expressed as a function of these new state variables or the control parameters (f, d_1,d_2). As there are the same number of (19)–(23) than of variables, the system can be solved

$$\frac{di_{\mathrm{LA}}(t)}{dt} = \frac{1}{L_X}\left[V_{\mathrm{ABA}}(t) + L_X\omega \cdot i_{\mathrm{LB}}(t) - V_{\mathrm{SA}}(t) - r \cdot i_{\mathrm{LA}}(t) - \frac{i_{\mathrm{LA}}(t) \cdot \sin^2[\psi(t)] + i_{\mathrm{LB}}(t) \cdot \mu(t)}{\pi \cdot \omega C_P}\right] \tag{19}$$

$$\frac{di_{\mathrm{LB}}(t)}{dt} = \frac{1}{L_X}\left[V_{\mathrm{ABB}}(t) - L_X\omega \cdot i_{\mathrm{LA}}(t) - V_{\mathrm{SB}}(t) - r \cdot i_{\mathrm{LB}}(t) + \frac{i_{\mathrm{LA}}(t) \cdot \mu(t) - i_{\mathrm{LB}}(t) \cdot \sin^2[\psi(t)]}{\pi \cdot \omega C_P}\right] \tag{20}$$

$$\frac{dV_{\mathrm{SA}}(t)}{dt} = \frac{1}{C_S}[i_{\mathrm{LA}}(t) + C_S\omega \cdot V_{\mathrm{SB}}(t)] \tag{21}$$

$$\frac{dV_{\mathrm{SB}}(t)}{dt} = \frac{1}{C_S}[i_{\mathrm{LB}}(t) - C_S\omega \cdot V_{\mathrm{SA}}(t)] \tag{22}$$

$$\frac{dV_{\mathrm{OAVG}}(t)}{dt} = \frac{1}{C_f}\left[\frac{i_{\mathrm{LP}}(t)}{\pi} \cdot (1 + \cos[\psi(t)]) - \frac{V_{\mathrm{OAVG}}(t)}{R}\right]. \tag{23}$$

3) The dynamic model expressed by (19)–(23) is not exact. It has been obtained through a harmonic approximation of variables. Nevertheless, the information it provides is still very accurate.
4) As the exact resonant current $i_L(t)$ has been approximated by a sinusoidal waveform, the information contained in the new state variables $i_{\mathrm{LA}}(t)$ and $i_{\mathrm{LB}}(t)$ is the magnitude (24) and phase (25) of that sinusoid. The same relation-

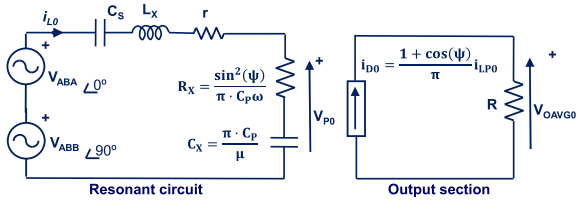

Fig. 7. Equivalent circuit for the topology under steady-state condition.

ship is applicable to $V_S(t)$ and $V_{SA}(t)$–$V_{SB}(t)$. On its side, $V_{OAVG}(t)$ represents the evolution along time of the average value of V_O(t) in a switching period

$$i_{LP}(t) = \sqrt{i_{LA}(t)^2 + i_{LB}(t)^2} \tag{24}$$

$$\varphi = Atan\left(\frac{i_{LB}(t)}{i_{LA}(t)}\right). \tag{25}$$

5) The model is suitable for any configuration of $V_{AB}(t)$. Fig. 6 presents two of the possibilities, and (15)–(18) provide the formulation of their respective first harmonic term which must be inserted in (19) and (29). If d_2 is made zero, the resulting model is applicable to the original PRC-LCC resonant converter with a capacitor as output filter.

V. Steady-State Model

The large signal model (19)–(23) of the topology contains a steady-state model. It is only necessary to consider the particular case where the variables do not change from one period to the next. Mathematically, this means that variable derivatives are zero. Making this assumption in (19)–(23), they provided the steady-state model, given in (26)–(30). The subscript 0 stands for static operation

$$Z_{REAL} = r + \frac{\sin^2[\psi_0]}{\pi \cdot \omega_0 C_P} \tag{26}$$

$$Z_{IMAG} = L_X \omega_0 - \frac{1}{\omega_0 C_S} - \frac{\mu_0}{\pi \cdot \omega_0 C_P} \tag{27}$$

$$i_{LA0} + j \cdot i_{LB0} = \frac{V_{ABA} + j \cdot V_{ABB}}{Z_{REAL} + j \cdot Z_{IMAG}} \tag{28}$$

$$V_{OAVG0} = R \cdot \frac{\sqrt{i_{LA0}^2 + i_{LB0}^2}}{\pi}(1 + \cos\psi_0) \tag{29}$$

$$\cos\psi_0 = \frac{\pi - 2R \cdot \omega_0 C_P}{\pi + 2R \cdot \omega_0 C_P}. \tag{30}$$

This model can be summarized in an equivalent circuit, Fig. 7, whose analysis provides the same set of equations (26)–(30). The circuit is divided into two meshes. On the left, an RLC circuit represents the resonant stage of the topology. Two sinusoidal power sources force the resonant current to flow. R_X stands as an equivalent resistance of the load seen from the low voltage side of the transformer, through the output rectifier. The power transferred to R_X is equal to the output power. On the right, a dc current source feeds the output section to compute the converters output voltage on the load *R*.

TABLE I
Value of *k* for Different Capacitors Ratios

β	1	1.5	2
k	4	3.4	3

VI. Discussion

The study of the steady-state model allows quantifying the maximum transferred power of the topology (31) for a wide set of different voltages gains. "*C*" is the serial association of C_P and C_S (32) while "*k*" is a constant, which depends on the capacitors ratio β (33). Usually, a good choice for β is in the range 1–2. Lower values of β lead to high voltages in the series capacitor and to a narrow distance between the series and the parallel resonances, where the converter must operate. Higher values of β imply too high series capacitances. In the middle of the range, $\beta = 1.5$ has been established for the design of the converter. Table I presents a relationship between "*k*" and β obtained from the steady-state model (see Fig. 7)

$$P_{MAX} = \frac{k \cdot V_{IN}^2}{\sqrt{\frac{L_X}{C}}} \tag{31}$$

$$C = \frac{C_S \cdot C_P}{C_S + C_P} \tag{32}$$

$$\beta = \frac{C_S}{C_P} \rightarrow \text{If } \beta = 1.5 \text{ then } C = 0.6 \cdot C_P. \tag{33}$$

On the other side, the minimum switching frequency is given by the series resonance of C_S and L_X (34). If the maximum transferable power and the minimum resonant frequency are known, an adequate value for the passive components of the resonant circuit can be deduced from (31), (33), and (34) – three equations and three variables

$$f_S = \frac{1}{2 \cdot \pi \cdot \sqrt{L_X \cdot C_S}}. \tag{34}$$

The PRC-LCC resonant converter is a particular case of the multilevel topology presented in this paper. Therefore, (31)–(34) also apply. If the goal is a maximum power of 100 kW and a minimum switching frequency of 50 kHz, a possible set of parameters for the topology passive components are: $L_S = 10\,\mu$H, $C_S = 950$ nF, and $C_P = 630$ nF. They ensure that maximum power is reachable at the minimum input voltage $V_{IN} = 400$ V. On the other side, L_S and C_P match the parasitics of the available stepup transformer. The transformer ratio is set to 1:133. Therefore, the intrinsic voltage gain (excluded the stepup transformer) of the topology is between 0.5 ($V_O = 50$ kV and $V_{IN} = 750$ V) and 2.8 ($V_O = 150$ kV and $V_{IN} = 400$ V), the most suitable range. The simulation results presented in Fig. 8 were obtained under these assumptions.

Fig. 8 considers a 100 kW design based on the PRC-LCC topology. A typical X-ray application will demand output voltages ranging from 50 to 150 kV. For $V_{IN} = 400$ V, quasi-ideal conditions, Fig. 3, are set approximately in the middle of the range, at 90 kV. Accordingly, $d = 0.43$ and $i_{LP} = 415$ A are obtained theoretically for those conditions in Fig. 8. Unfortunately,

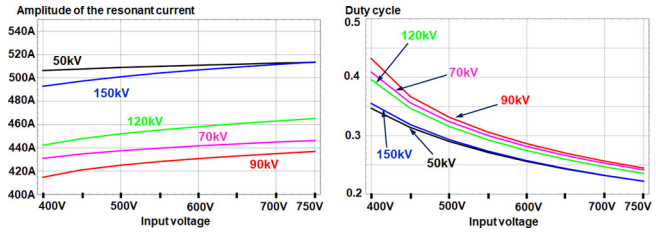

Fig. 8. Expected resonant current and duty cycle evolution when the input voltage changes from 400 V to 750 V in the PRC-LCC with a capacitor as output filter. Every curve represents a different output voltage at a constant output power of 100 kW.

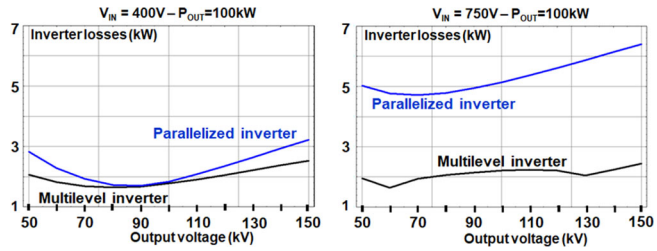

Fig. 9. Losses in the eight switches of the inverter, left $V_{\rm IN} = 400$ V, right $V_{\rm IN} = 750$ V when output power is 100 kW.

for other output voltages, the control parameters, switching frequency f and duty cycle d must change, even if $V_{\rm IN}$ continues to be 400 V. The control scheme of Fig. 4(c) was followed during the calculations to minimize circulating energy. No matter the choice, less favorable conditions for current and duty cycle are obtained, reaching $d = 0.35$ and $i_{\rm LP} = 510$ A in the extremes of the output voltage range.

If the input voltage is increased from 400 V upwards, Fig. 8 shows that the current amplitude does not diminish, as it would be desirable. Actually, it even experiments a slight increment. To keep power balance, duty cycle drops clearly with a rising $V_{\rm IN}$. The situation becomes dreadful at $V_{\rm IN} = 750$ V. There, the duty cycle is around 0.25. It means that the switching transitions in the switches of the inverter occur at the worst moment of the period, when the resonant current is at its peak, $iL(t) = i_{\rm LP}$, Fig. 4(c). Moreover, expected values for that current peak and for the inverter voltage are at their maximums (440–510 A and 750 V, respectively, in the 100 kW example). Thus, switching transitions deal with the higher voltage and current levels, while the conduction losses are not reduced. It is not easy to find a switch for those power levels at high frequency. At least two switches must be connected in parallel to share the losses, assembling two inverters de facto. Si IGBTs is the usual choice for these current levels, more than 500 A. The use of a single 600 A or two 300 A IGBTs per switch produces unbearable losses beyond 1400 W per IGBT. However, SiC MOSFETs are arising as a promising alternative for currents up to 300 A, (CAS300M12BM2, from Cree) offering lower switching and conduction losses than their Si counterparts. Two of these MOSFETs can be parallelized for the application. An estimation of turn OFF and conduction losses for the couple is made following the method described in [29]. So, (35) and (36) are deduced, respectively, for switching and conduction losses calculation in the switches. To apply (36), the voltage of the MOSFET must be modeled. During a switching period, this voltage depends on the particular state of the switch (forward conduction, reverse MOSFET, reverse diode, and MOSFET). Using MOSFETs datasheet it is possible to adjust linearly the curves of the device to obtain "a" and "b" in (36) for every case. Now, the model of the topology provides data for the waveforms in any particular operation point, i.e., frequency, duty cycle, current, and different transition angles between regions in the switch, "$\alpha 1$" and "$\alpha 2$" [17]. Joining the information from the models, the total losses for the parallelized inverter can be calculated, Fig. 9. The accuracy of this method has been proved experimentally many times as, for example, in [30] and [31]. In particular, Villegas *et al.* [30] compare theoretical and experimental losses in an 80 kW inverter like the one presented in Fig. 2 with similar conclusions. As expected, for $V_{\rm IN} = 750$ V and $P = 100$ kW, losses increase dramatically due to duty cycles close to 0.25, Fig. 9, getting to a 7% (7 kW!) of total transferred power. As a result, a big amount of losses is expected in this configuration of the inverter, even considering that the parallelization of the switches is perfect. In fact, this is an additional issue, with many problems to solve from the dynamical and static point of view, involving a careful design of the drivers and a slowdown of switching transitions for equalization

$$P_{\rm off} = 2E_{\rm off}\frac{I}{I_N}\frac{V}{V_N}f = 2 \cdot 5\ {\rm mJ}\frac{260}{300}\frac{750}{600}80\ {\rm kHz} = 866\ {\rm W} \tag{35}$$

$$P_{\rm COND} = \int_{\alpha_1}^{\alpha_2} I \cdot \sin(\omega t) \cdot [a \cdot I \cdot \sin(\omega t) + b]\, dt. \tag{36}$$

The proposed multilevel strategy introduces some flexibility in the scheme. Now it is possible to establish $V_{\rm IN} = 800$ V as the minimum input voltage, because in the extreme, when $V_{\rm IN} = 400$ V, a square voltage of 800 V could be obtained using both inverters. Thus, the strategy is to use an inverter voltage as the one in Fig. 6(b) to compensate variations in the input in the way that the first harmonic of $V_{\rm AB}$ will always be equivalent to the 800 V case. Now, since $V_{\rm IN}$ is higher because the presence of two inverters, the transformer ratio n is lowered to 1:70, and the intrinsic voltage gain of the topology is restricted to 0.95–2.85. On the other hand, a higher minimum input voltage affects the suitable values of the passive components. According to (31)–(34), those new values should be about $L_S = 35\ \mu$H, $C_S = 275$ nF, and $C_P = 183$ nF. An important aspect of the situation is that the parasitic capacitance, C_P, and leakage inductance, L_S, of the stepup transformer are mainly in its secondary side whose number of turns and isolation distances to the core must be quite bigger to generate and withstand kV. Of course, a reduction in the transformer ratio affects the value of parasitics when observed from the primary. In fact, L_S is multiplied for $(133/70)^2$ and C_P is divided by the same quantity. Therefore, it is possible to modify just the primary of the transformer and to obtain the newly desired parasitics on it. Additionally, this new primary will occupy more or less the same volume in the core

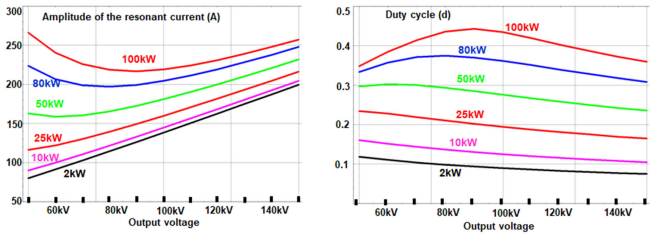

Fig. 10. Theoretical current and duty cycle in the multilevel structure when the voltage in the input is 750 V.

window, since the number of turns is almost doubled but, as later demonstrated, the current is going to be halved. Hence, the changes for a new suitable transformer looks not only feasible, but also minor.

Fig. 10 shows the current peak for iL and the required duty cycle d1 to reach different output voltages and powers with the new proposed multilevel topology. The maximum expected current is 260 A, half the calculated before, Fig. 8. This is coherent to the application of $V_{\rm IN} = 800$ in (1) and to a narrower range in the intrinsic voltage gain.

Fig. 10 can help to estimate the turn OFF switching losses in one of the switches. For $V_{\rm IN}$ equal to 750 V, the model predicts the worst case when the output power is 50 kW and the output voltage is 150 kV. In this situation, the expected current, with an amplitude of 240 A, is switched at its peak, since the duty cycle under these conditions is 0.25. According to (35), worst-case switching losses are reduced to 400 W, half the amount previously computed, because of current diminution. At 750 V, only one of the inverters is active, working with d1 close to 0.25. The other is short-circuited, ideally $d_2 = 0$. However, both inverters can change papers in alternate periods, sharing switching losses between them. The expected turn OFF losses per switch are reduced to 200 W in the bad leg of the inverters. Turning ON losses are not so important since they occur with low current, Fig. 6(b). On the other hand, the diminution of the current to a half, from 540 A to 260 A, ensures a favorable situation also for conduction losses in the multilevel structure. Additionally, it is easier to find switches with a suitable current rate, and the problems of parallelizing are avoided. Fig. 9 compares the losses of the proposed multilevel inverter at 100 kW against a parallelized full bridge with perfect current sharing. Now, total conduction and switching losses are below 3% of full power, independently of the input voltage. These new calculations are made using the same switch and considering the proposed models for losses [29]–[31]. With the proposed structure, the reduction in the inverter losses is huge, a 50% when $V_{\rm IN} = 750$ V. Any inaccuracy in the calculations is belittled by this fact. In the multilevel topology, for rated power, one of the inverters is programmed with d1 close to 0.5 while d_2 is used for power regulation. As power diminishes, d_2 diminishes as well, fetching eventually zero. At that moment, d_1 is used to regulate power. In this way, one of the inverters is always under good switching conditions, in phase with the resonant current i_L. This diminishes switching losses, which might even be equalized between inverters if they are used alternatively to host d_1 and d_2. For a given amount of

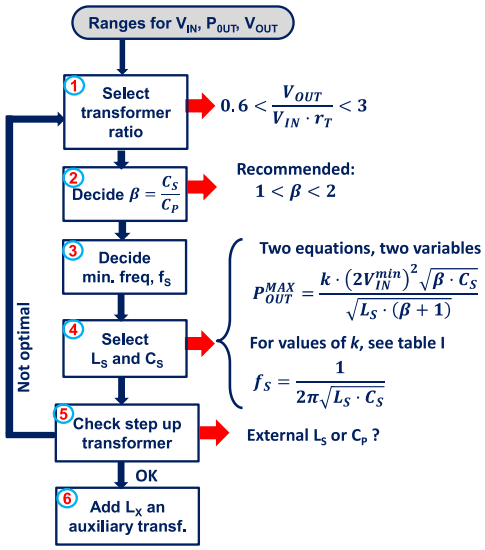

Fig. 11. Small flowchart to adapt the topology for a given application.

power, the resonant nature of the structure makes the current remain almost invariable, independently of the input voltage. Obviously, lower the input voltage more relaxed the switches. Thus, Figs. 9 and 10 calculated for maximum $V_{\rm IN}$ depict worst operating conditions.

The mathematical model makes up a great tool to program a digital control. For a given output voltage and power, the model is capable to compute the required switching frequency and duty cycles, $d_1 - d_2$ (see the Appendix). Moreover, following the method described in [13], a simple polynomial model, easy to program, might also be developed for this topology. These calculations provide a good starting point to switch the converter ON. Then, a linear control is enough to adjust accurately these parameters. In fact, as many other converters whose output filter is made with only a capacitor, the dynamic response of the topology is first order [16], [17], [30]. The model is also a good tool to adapt the converter design to a given application. Fig. 11 depicts in a flowchart the steps that should be followed for that purpose.

VII. Experimental Verification of the Model

The precedent mathematical analysis is validated with a scaled prototype. The scale of voltage was established to a tenth of a three-phase rectified the main line: 40 V $\leq V_{\rm IN} \leq$ 75 V. The resonant circuit is the same as calculated in the previous paragraph. Thus, a scale of 1–10 and 1–100 appears for current and power levels in the converter, respectively. On the other hand, a dead time of 600 ns is established between the switches of the same inverter branch. This value, typical of large current transistors, limits the maximum reachable d_1. In the prototype, it has not been programmed larger than 0.43. Additionally, switching transitions cannot occur when the resonant current is exactly zero. A minimum circulating current is required to charge and discharge the capacities of the witches. Using the mathematical model, this time is fixed in the prototype to 500 ns. This delay in current zero crossing limits the short-circuiting of the auxiliary

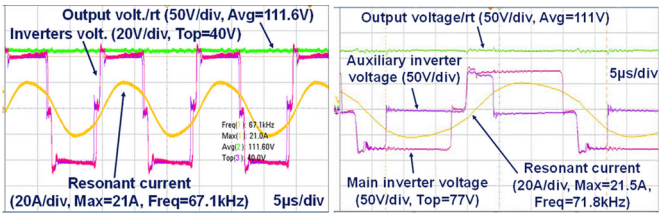

Fig. 12. Experimental measurement of a critical point: 1 kW at 8 kV. On the left, the minimum $V_{\mathrm{IN}} = 40$ V requires maximum d1 and d2 to obtain full power. On the right with $V_{\mathrm{IN}} = 75$ V one of the inverters works with lower duty cycle. The current peak is around 21 A in both cases, as the model predicted.

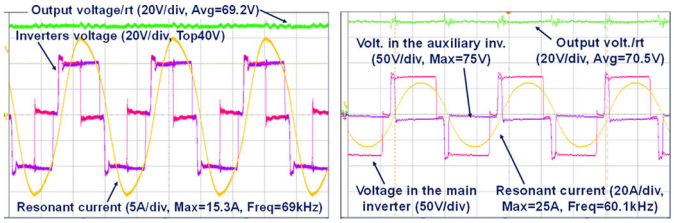

Fig. 13. Experimental measurement with 1 kW, 5 kV at the output. On the left $V_{\mathrm{IN}} = 40$ V and d2 = 0.23: the auxiliary inverter is switching OFF at maximum current. On the right, $V_{\mathrm{IN}} = 75$ V. In both cases the main inverter mantains d1 close to 0.4 and the resonant current has the predicted moderated value, 15.3 A and 25 A.

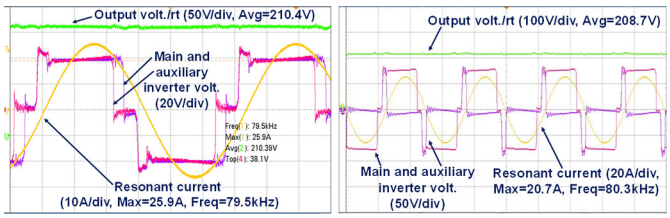

Fig. 14. Experimental measurement at 1 kW, 15 kV. On the left $V_{\mathrm{IN}} = 40$ V requires large duty cycles in both inverters. On the right, $V_{\mathrm{IN}} = 75$ V, only the main inverter is providing voltage. In both cases, as the model predicts, the resonant current is similar, around 25 A.

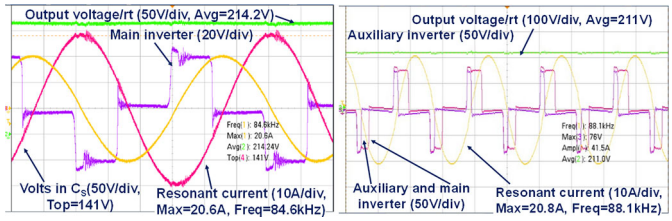

Fig. 15. Experimental measurement at 50 W, 15 kV. Although power is reduced to a twentieth, resonant current amplitude is still above 20 A, similar to full power levels, as predicted by the model. On the left $V_{\mathrm{IN}} = 40$ V, on the left $V_{\mathrm{IN}} = 75$ V.

TABLE II
AVERAGE ERRORS OBTAINED

i_{LP}	V_S	d_1	d_2
5%	2.7%	0.01	0.02

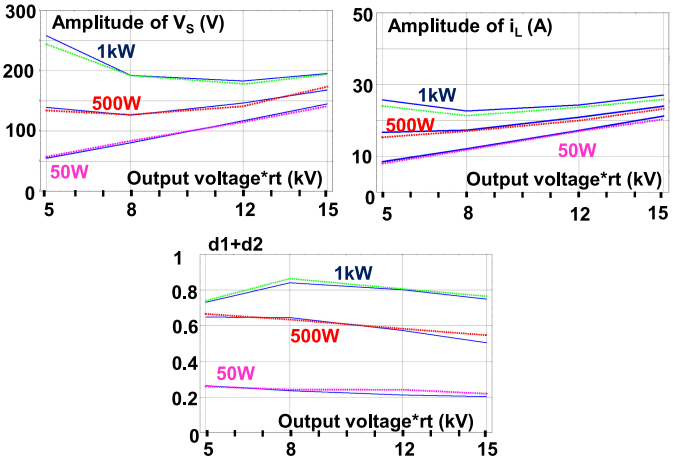

Fig. 16. Example of the difference between the theoretical prediction and the experimental measurement in the 1:10 prototype.

inverter, forcing the conduction of the antiparallel diodes during it. A minimum d_2 appears in the current transitions. Although the exact value depends on the switching frequency, it is always very similar to 0.04. Losses when d_2 is minimum are not large, since the transitions in the switches of the auxiliary inverter take place under a very small amount of current, Fig. 15, while the diodes switch ON and OFF under zero volts.

The experimental results obtained in the prototype were consistent with the predictions of the model. As an example, Figs. 12–15 represent the main waveforms for rated power and one-twentieth of full power at different output voltages, respectively. Every output condition has been obtained in the extremes of the input voltage range, 40 V and 75 V, while the output voltage was measured reflected to primary (transfer ratio $r_t = 1{:}70$). CH1, yellow, represents the resonant current i_L, CH2, green, the reduced output voltage, V_0, CH3, and CH4 the main, V_A, and auxiliary, V_B, inverter voltages, respectively.

Figs. 12–15 show that the maximum current in the inverter is 26 A (260 A, 100 kW, 150 kV in the 1:1 prototype) as predicted by the model. As the model also predicts, this current does not diminish with power. In Fig. 14, it is still as high as 20 A for only 50 W (200 A, 5 kW in the 1:1 prototype). Other interesting property of the proposed topology is that the peak current is never going to be simultaneously switched by both inverters. Together with the diminishing of current amplitude, this fact leads to a better performance in switching losses.

As a summary of the model accuracy, Table II shows a calculation of the average errors found between theoretical and measured magnitudes. With the same purpose, Fig. 16 shows a comparison between the actual measurements in the prototype (dashed lines) and the results predicted by the model (solid lines) for $V_{\mathrm{IN}} = 40$ V. The measurements are done at rated power, 1 kW, half power, 500 W, and one-twentieth of full power, 50 W.

VIII. FLUOROSCOPY MODE

Unlike radiography (kW and milliseconds), in fluoroscopy, the power levels are low and the operation time is long, even half an hour. However, the same power supply is expected to

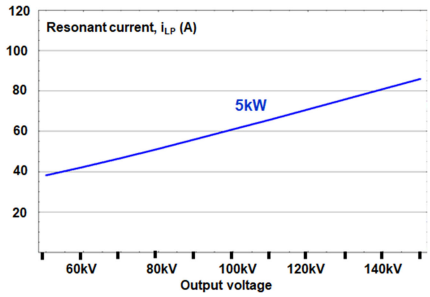

Fig. 17. Theoretical current for low power when the auxiliary inverter is left open.

feed the X-ray tube under such so different conditions. Adapting a 100 kW source to deliver 2 kW is not simple. Fig. 10 shows one of the major drawbacks of resonant topologies: the resonant current does not diminish proportionally to delivered power. At 2 kW, circulating current can reach up to 200 A, which is confirmed in an experimental prototype in Fig. 15. Obviously, this has an impact on efficiency and heatsink size. The origin of this problem is in the parallel capacitor C_P. It must be charged and discharged every period to the output voltage, Fig. 6. Therefore, the minimum required current for that depends on frequency and output voltage (37). In fact, Fig. 10 shows a linear dependence of the current with the output voltage for low power. It does not help either that the way to diminish power in resonant converters is to increase the frequency

$$i_L^{\min} = \omega \cdot C_P \cdot V_o. \tag{37}$$

There are only two possibilities to diminish circulating current at low power: to diminish C_P or to diminish ω. However, lowering C_P is difficult, affects transferable power (31) and is not too effective since it leads to an increment in the parallel resonance and therefore in the switching frequency in the following equation:

$$f_P = \frac{1}{2 \cdot \pi \cdot \sqrt{L_X \cdot \frac{C_S \cdot C_P}{C_S + C_P}}}. \tag{38}$$

This paper proposes the increment in L_X for low power. It will cause a diminishing in f_P (38) and f_S (34), and hence in the switching frequency. Regarding (31) the increment in L_X also causes a decrement in maximum transferable power, but the measure is intended for low power levels. The multilevel topology inserts easily and additional inductance in the resonant circuit if the secondary inverter is disconnected from the circuit. Now the main inverter is operating alone to deliver power and the magnetizing inductance of the auxiliary transformer is added to the resonant net. This magnetizing inductance can be designed on purpose to meet low power level requirements. For our example, L_M is set to 180 μH, what reduces the switching frequency and the circulating current more than a half (34)–(38), Fig. 17. This has a big impact on losses. The impact could be even greater if the magnetizing inductance, L_M, of the auxiliary transformer were even bigger. For instance, L_M equal to 250 μH will reduce frequency and current to a third. The designer must consider the implications in size and cost of such a decision.

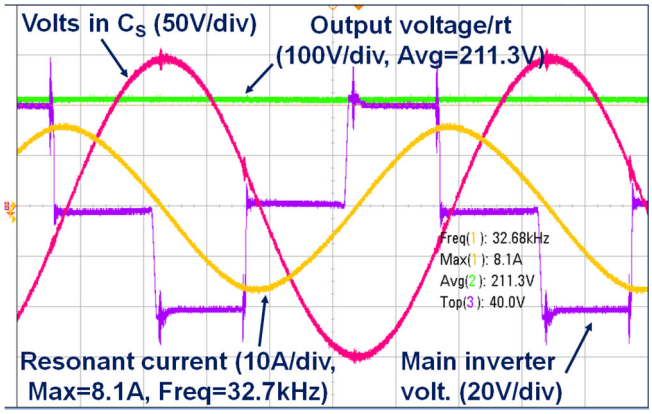

Fig. 18. Experimental measurement at 50 W, 15 kV with only one inverter. Resonant current is 2.5 times lower. In the picture, d1 = 0.22.

Fig. 18 shows an experimental measurement of the low power delivered in these conditions. It has been obtained for the same output power and voltage presented in Fig. 15 where both inverters are active. As predicted by the model, the resonant frequency and current has diminished considerably, from 20.3 A to 8.1 A (from 203 A to 81 A in the 1:1 scale). Switching, magnetic, and resistive losses in the inverter and the transformer are also reduced since frequency lowers from 85 kHz to 32.7 kHz. Again, the model of the topology provides an accurate calculation with a 6% error in i_{LP} and 0.02 in d_1.

IX. Conclusion

For high power, high output voltage dc power supplies, the use of resonant converters is very convenient. However, beyond 50 kHz and 70 kW, current levels are so high that it is necessary to connect two switches in parallel to withstand losses. This implies many problems as to synchronize the drivers of the parallelized transistors or to equalize them dynamically. In this paper, with the same quantity of switches, an alternative structure has been proposed, modeled, and evaluated. The accuracy of the topology model has been proved by experimentation. The paper also includes an algorithm to dimension and design the proposed topology for a particular application, being the scaled prototype, Fig. 19, a good implementation of a particular case.

The multilevel configuration supports two different duty cycles. The cost is an additional 1:1 auxiliary transformer. With a more flexible control, the topology model predicts, and the scaled prototype shows, that it is easier to deal with the wide input voltage variations inherent to the three-phase main line standards: 400 V to 750 V dc. In fact, the design of the resonant net can be adapted to a scene where the input voltage can be considered the maximum of the range, 800 V. As consequence, it has been experimentally verified that the maximum resonant current is reduced to a half, with benefits in inverter switching and conduction losses, proposing SiC MOSFET as the switch of choice. In particular, for input voltages close to the upper end of the range, only one inverter is switching the halved current, having the possibility to reduce drastically switching losses. The

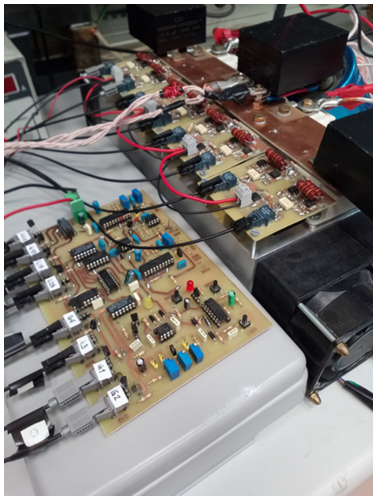

Fig. 19. Picture of the prototype.

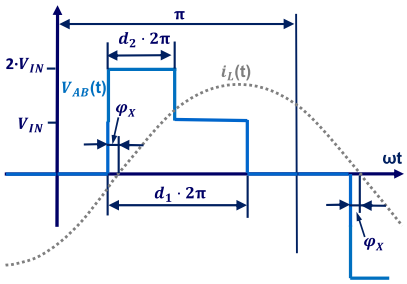

Fig. 20. Optimal switching. One leg of each inverter conmutates with very low inductive current.

strategy to operate different inverters in alternate periods also improves losses sharing between switches.

Additionally, the magnetizing inductance of the 1:1 auxiliary transformer can be used to modify the resonant net in low power conditions. It has been experimentally proved in a scaled prototype that the resonant current and the switching frequency are largely reduced by this fact. Thus, the benefits of small size in high power design and low losses in low power but long time operating conditions are combined.

This multilevel structure can be extended to three or more inverters connected through two or more additional transformers in case than larger power levels were necessary.

APPENDIX

This appendix illustrates how to obtain the value of the control variable values: f, d_1, and d_2, for a target output power P_0 and voltage V_0 when operating in optimum switching mode, Fig. 20. The mathematical formulation of the model comprises a transcendental equation. Therefore, an iterative process is proposed as simple solution. Regarding the topology equivalent circuit, Fig. 7, (A1) represents the KVL for the resonant section, where V_{AB}, i_L, and Z are function of the control variables that must be calculated. In fact, V_{AB} depends on d_1 and d_2, (17), (18) and Z depends on f (26), (27), and (30)

$$V_{\mathrm{ABA}} + j \cdot V_{\mathrm{ABB}} = (i_{\mathrm{LA}} + j \cdot i_{\mathrm{LB}}) \cdot (Z_{\mathrm{REAL}} + j \cdot Z_{\mathrm{IMAG}}). \tag{A1}$$

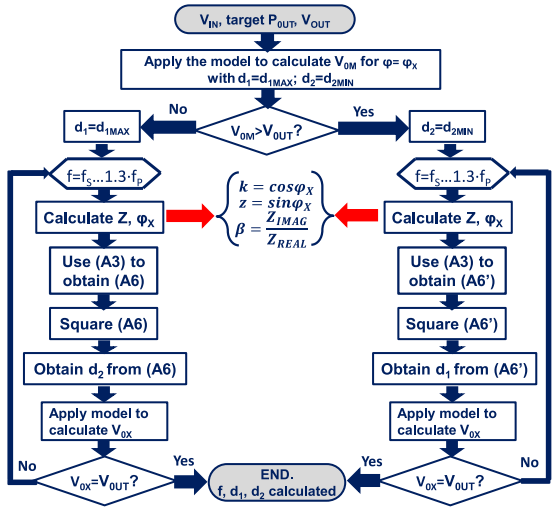

Fig. 21. Algorithm to calculate the optimum control parameters for a target operating point.

1) The iteration consist in a sweep of frequency values, from the minimum, f_S, (34) to a maximum, 1.3 times f_P (38). A "for" loop implements the sweep. Once f has a value, Z can be computed in (A1).
2) Regarding the current, optimal switching mode means a minimum phase between current and inverter voltage φ_X, Fig. 20. In fact, φ_X is defined from the switching time in the MOSFET (some nanoseconds, ideally zero), and translated to angle via the switching frequency f. Once φ_X is known, a new condition is set for the current real and imaginary parts (A2). Combining (A1) and (A2) originates (A3)

$$\begin{aligned} &i_{lA}\cos(\pi d_1 - \varphi_X) + i_{lB}\sin(\pi d_1 - \varphi_X) \\ &\quad = i_{lA}a + i_{lB}b = 0 \end{aligned} \tag{A2}$$

$$\begin{aligned} &Z_{\mathrm{REAL}}(aV_{\mathrm{ABA}} + bV_{\mathrm{ABB}}) \\ &\quad + Z_{\mathrm{IMAG}}(-bV_{\mathrm{ABA}} + aV_{\mathrm{ABB}}) = 0. \end{aligned} \tag{A3}$$

3) As V_{ABA} and V_{ABB} depend on d_1 and d_2, (A3) is a function of d_1 and d_2. However, the control strategy helps to fix one of these variables: at large power d_1 is fixed to a maximum (0.45 for instance) while d_2 varies, and at low power d_2 is fixed to a minimum (0.05 for instance) while d_1 varies. This means that, in the end, (A3) is a function of just one variable, d_1 or d_2. Therefore, it can be solved. The procedure to obtain this remaining variable is simple but long, Fig. 21.
4) For instance, if d_1 is known, the only variable is d_2. Now, it is possible to define four constants (k, z, c, s) given as an array in (A4). Trigonometry helps to reduce "a" and "b"

from (A2) to those constants, (A5)

$$\begin{pmatrix} \cos\varphi_X & \sin\varphi_X \\ \cos\ (\pi d_1) & \sin\ (\pi d_1) \end{pmatrix} = \begin{pmatrix} k & z \\ c & s \end{pmatrix} \tag{A4}$$

$$a = c \cdot k + s \cdot z; \quad b = s \cdot k - c \cdot z. \tag{A5}$$

5) Joining (17), (18), (A4), and (A5), (A3) is transformed into (A6). (A6) is a trigonometric equation where d_2 appears as the only unknown variable. To solve (A6), a possibility is to square both sides of the equation and to substitute $\sin^2(2\pi d_2)$ by $1 - \cos^2(2\pi d_2)$. The result is a second order linear equation that can be easily solved for $\cos(2\pi d_2)$ and hence for d_2 as it was the initial target. Of course, a second order equation provides two solutions. To choose between them it is enough to remember that $0 \leq d_2 \leq 0.5$

$$\sin(2\pi d_2) = \frac{\cos(2\pi d_2)\left[z - k \cdot \beta\right] + k\left[2s^2\beta + \beta - 2cs\right] - z\left[2s^2 + 2cs\beta + 1\right]}{k + \beta \cdot z}. \tag{A6}$$

In the other case, if d_2 is known, the procedure to obtain d_1 is identical. The only differences are that constants "c" and "s" will depend on d_2 and that (A6) will change to show a dependence on $\sin(2\pi d_1)$ and $\cos(2\pi d_1)$.

6) At this moment, d_1 and d_2 have been calculated to be on the optimal switching mode for the frequency selected in the "for" loop. The equations of the model (26)–(29) are used to compute the output voltage V_0. If it is not the one defined as a target, a new value of f is taken, otherwise, the iteration has finished. This calculation model is explained graphically in Fig. 21.

The described algorithm has been successfully implemented in a mathematical environment. Gathering different operating points, the curves that describe the topology behavior have been obtained with this process. In a further step, these curves can be approximated by polynomials [13]. This simplifies the calculation for an embedded digital control.

REFERENCES

[1] Z. Haifeng and W. Peng, "Design of an LCC resonant converter for furnace power supply during electron beam melting," *IEEJ J. Ind. Appl.*, vol. 6 no. 6, pp. 387–394, 2016.

[2] D. Siemaszko, S. Pittet, D. Aguglia, and L. de Mallac, "Design of a modular resonant converter for 25 kV-8 A DC power supply of RF cavities," in *Proc. 2014 Int. Power Electron. Conf.*, Hiroshima, Japan, 2014, pp. 3371–3378.

[3] G. Ning *et al.*, "Hybrid resonant ZVZCS PWM full-bridge converter for large photovoltaic parks connecting to MVDC grids," *IEEE J. Emerg. Sel. Topics Power Electron.*, vol. 5, no. 3, pp. 1078–1090, Sep. 2017.

[4] S. D. Johnson, A. F. Witulsky, and R. W. Erickson, "A comparison of resonant topologies in high voltage DC applications," *IEEE Trans. Aerosp. Electron. Syst.*, vol. 24, no. 3, pp. 263–274, May 1988.

[5] S. N. Vukosavič and L. S. Perič, "A novel power tonverter topology for electrostatic precipitators," *IEEE Trans. Power Electron.*, vol. 31, no. 1, pp. 152–164, Jan. 2016.

[6] X. Sun, X. Li, Y. Shen, B. Wang, and X. Guo, "Dual-bridge LLC resonant converter with fixed-frequency PWM control for wide input applications," *IEEE Trans. Power Electron.*, vol. 32, no. 1, pp. 69–80, Jan. 2017.

[7] Z. De Greve, O. Deblecker, and J. Lobry, "Numerical modeling of capacitive effects in HF multiwinding transformers – Part I: A rigorous formalism based on the electrostatic equations," *IEEE Trans. Magn.*, vol. 49, no. 5, pp. 2017–2020, May 2013.

[8] J. Biela and J. W. Kolar, "Using transformer parasitics for resonant converters—A review of the calculation of the stray capacitance of transformers," *IEEE Trans. Ind. Appl.*, vol. 44, no. 1, pp. 223–233, Jan. 2008.

[9] P. Ranstad and H. P. Nee, "On the distribution of AC and DC winding capacitances in high frequency transformers with rectifier loads," *IEEE Trans. Ind. Electron.*, vol. 58, no. 5, pp. 1789–1798, May 2011.

[10] R. L. Steigerwald, "A comparision of half-bridge resonant converter topologies," *IEEE Trans. Power Electron.*, vol. 3, no. 2, Apr. 1988.

[11] S. D. Johnson, A. F. Witulsky, and R. W. Erickson, "A comparison of resonant topologies in high voltage DC applications," *IEEE Trans. Aerosp. Electron. Syst.*, vol. 24, no. 3, May 1988.

[12] A. K. S. Bhat, "Analysis and design of a series parallel resonant converter with capacitive output filter," *IEEE Trans. Ind. Appl.*, vol. 27, no. 3, pp. 523–530, Jun. 1991.

[13] J. Martín-Ramos, J. Díaz, F. Nuño, P. j. Villegas, A. López, and J. F. Gutiérrez, "A polynomial model to calculate steady-state set point in the PRC-LCC topology with a capacitor as output filter," *IEEE Trans. Ind. Appl.*, vol. 51, no. 3, pp. 2520–2527, May 2015.

[14] J. Martin-Ramos, A. M. Pernía, J. Diaz, F. Nuño, and J. A. Martínez, "Power supply for a high voltage application," *IEEE Trans. Power Electron.*, vol. 23, no. 4, pp. 1608–1619, Jul. 2008.

[15] C. Iannello, S. Luo, and I. Batarseh, "Full bridge ZCS PWM converter for high-voltage high-power applications," *IEEE Trans. Aerosp. Electron. Syst.*, vol. 38, no. 2, pp. 515–526, Apr. 2002.

[16] G. Ivensky, A. Kats, and S. Ben-Yaakov, "An RC load model of parallel and series parallel DC-DC converters with capacitive output filter," *IEEE Trans. Power Electron.*, vol. 14, no. 3, pp. 515–521, May 1999.

[17] J. Martin-Ramos, J. Diaz, A. M. Pernía, J. M. Lopera, and F. Nuño, "Dynamic and steady state models for the PRC-LCC topology with a capacitor as output filter," *IEEE Trans. Ind. Electron.*, vol. 54, no. 4, pp. 2262–2275, Aug. 2007.

[18] R. Yang, H. Ding, Y. Xu, L. Yao, and Y. Xiang, "An analytical steady state model of LCC type series-parallel resonant converter with capacitive output filter," *IEEE Trans. Power Electron.*, vol. 29, no. 1, pp. 328–338, Jan. 2014.

[19] S. Gavin, M. Carpita, P. Ecoeur, H. P. Biner, M. Paolone, and E. T. Louokdom, "A digitally controlled 125 kVdc, 30 kW power supply with an LCC resonant converter working at variable DC-link voltage: Full scale prototype test results," in *Proc. 7th IET Int. Conf. Power Electron., Mach. Drives*, 2014, pp. 1–6, doi: 10.1049/cp.2014.0297.

[20] M. Hu, N. Froehlekw, W. Peters, and J. Boecker, "Multi-objective optimization of LCC resonant converter applied in VLF HV generator," in *Proc. 37th Annu. Conf. IEEE Ind. Electron. Soc.*, Nov. 2011, pp. 1456–1461.

[21] J. Martin-Ramos, P. J. Villegas, A. M. Pernía, J. Díaz, and J. A. Martinez, "Optimal control of a high voltage power supply based on the PRC-LCC topology with a capacitor as output filter," *Trans. Ind. Appl.*, vol. 49, no. 5, pp. 2323–2329, May 2013.

[22] R. Casanueva, C. Brañas, F. J. Azcondo, and F. J. Díaz, "Teaching resonant converters: Properties and applications for variable loads," *IEEE Trans. Ind. Electron.*, vol. 57, no. 10, pp. 3355–3363, Oct. 2010.

[23] N. Shafiei, M. Pahlevaninezhad, H. Farzanehfard, and S. R. Motahari, "Analysis and implementation of a fixed-frequency LCLC resonant converter with capacitive output filter," *IEEE Trans. Ind. Electron.*, vol. 58, no. 10, pp. 4773–4782, Oct. 2011.

[24] J. A. Martín-Ramos, Ó. Pardo-Vaquero, P. J. Villegas, J. A. Martínez, and A. M. Pernía, "Multilevel PRC-LCC resonant converter for X-ray generation," *IET Electronic Lett.*, vol. 51, no. 15, pp. 1189–1191, Jul. 23, 2015.

[25] W. C. Hsu, J. F. Chen, Y. P. Hsieh, and Y. M. Wu, "Design and steady-state analysis of parallel resonant DC–DC converter for high-voltage power generator," *IEEE Trans. Power Electron.*, vol. 32, no. 2, pp. 957–966, Feb. 2017.

[26] A. K. Singh, P. Das, and S. K. Panda, "Analysis and design of SQR-based high-voltage LLC resonant DC–DC converter," *IEEE Trans. Power Electron.*, vol. 32, no. 6, pp. 4466–4481, Jun. 2017.

[27] S. R. Sanders, J. M. Noworolski, X. Z. Liu, and G. Verghese, "Generalized averaging method for power conversion circuits," *IEEE Trans. Power Electron.*, vol. 6, no. 2, pp. 251–259, Apr. 1991.

[28] E. X. Yang, F. C. Lee, and M. M. Jovanovic, "Extended describing function technique applied to the modelling of resonant converters" VPEC, 1991.
[29] D. Graovac, M. Pürschel, and A. Kiep, MOSFET Power Losses Calculation Using the Data-Sheet Parameters Infineon Technologies, 2006.
[30] P. J. Villegas, J. A. Martín-Ramos, J. Díaz, J. A. M. Esteban, M. A. J. Prieto, and A. M. Pernía, "A digitally controlled power converter for an electrostatic precipator," *Energies*, vol. 10, no. 12, Dec. 2017, Art. no. 2150.
[31] K. Filsoof and P. W. Lehn, "A bidirectional modular multilevel DC–DC converter of triangular structure," *IEEE Trans. Power Electron.*, vol. 30, no. 1, pp. 54–64, Jan. 2015.

Juan A. Martín-Ramos (M'99) received the M.Sc. and Ph.D. degrees in industrial engineering from the Universidad de Oviedo, Oviedo, Spain, in 1996 and 2001, respectively. In 1997, he joined the University of Oviedo as a Lecturer in the electronic technology area.

During this time, he has been involved in several R+D projects in different topics, ranging from microprocessor-based systems to the design of power supplies. His work has been focused on finding new and better solutions to industrial applications and the technology transfer from academia to industry. His current research interests include the design of magnetic components, and the conception of high voltage (hundreds of kV) medium power (tens of kW) power supplies. He has authored patents and technical papers on these topics.

Óscar Pardo-Vaquero received the M.Sc. and Ph.D. degrees in industrial engineering from the University of Oviedo, Oviedo, Spain, in 2004 and 2014, respectively.

His doctoral thesis was focused on new multilevel solutions for high voltage power supplies capable to deliver more than 100 kW. Since 2005, he has been working as a Process Engineer with a steel manufacturing company. His work deals with improving performance of rolling processes to increase quality properties of steel.

Juan Díaz (M'02) received the M.Sc. and Ph.D. degrees in electrical engineering from the University of Oviedo, Oviedo, Spain, in 1990 and 1995, respectively.

Since 1990, he is a Lecturer with the University of Oviedo. His research interests include switching-mode power supplies, resonant power conversion, piezoelectric transformers, dc high voltage applications, and the design of microcontrollers-based systems.

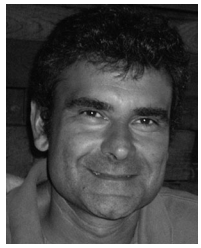

Fernando Nuño (M'96) was born in Asturias, Spain, in 1963. He received the M.Sc. and Ph.D. degrees in industrial engineering from the University of Oviedo, Oviedo, Spain, in 1988 and 1991, respectively.

He is currently a Full Professor in electronics with the University of Oviedo. His research interests include switching-mode power supplies, resonant power conversion, thermal modelling, design of magnetic devices, piezoelectric transformers, and design of digital embedded systems.

Pedro José Villegas (M'96) was born in Suances, Cantabria, Spain, in 1965. He received the M.Sc. and Ph.D. degrees in electrical engineering from the University of Oviedo, Gijón, Spain, in 1991 and 2000, respectively.

Since 2003, he has been an Associate Professor in the electronic technology area with the University of Oviedo. He has been involved in diverse power electronics research and development projects. He has authored several papers in international electronics conference proceedings and international journals. His research interests include switching-mode power supplies, converter modelling, high-power-factor rectifiers, and high power–high voltage power supplies.

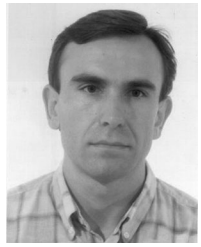

Alberto Martín-Pernía (M'97) was born in Cantabria, Spain, in 1964. He received the M.S. and Ph.D. degrees in electrical engineering from the University of Oviedo, Oviedo, Spain, in 1991 and 1996, respectively.

Since 1992, he has been working as an Associate Professor in the electronic technology area with the University of Oviedo. He has worked on different topics related with the power electronics and especially on high frequency power supply systems. He has several papers in international conferences and journals related to magnetic component integration and high power density dc/dc converters. His research interests include electronic instrumentation applied to biomedical systems, high output voltage converters, and the modelling of magnetic structures.